



# Effect of processing route on the properties of LSCF-based composite cathode for IT-SOFC

AAKASH AHUJA<sup>1</sup>, MANOJ GAUTAM<sup>1</sup>, AMIT SINHA<sup>2,\*</sup>, J SHARMA<sup>2</sup>, P K PATRO<sup>2</sup>  
and A VENKATASUBRAMANIAN<sup>1</sup>

<sup>1</sup>School of Energy and Environment, Thapar University, Bhadson Road, Patiala 147001, India

<sup>2</sup>Powder Metallurgy Division, Materials Group, Bhabha Atomic Research Centre, Vashi Complex, Navi Mumbai 400703, India

\*Author for correspondence (asinha@barc.gov.in)

MS received 16 September 2019; accepted 13 December 2019; published online 21 May 2020

**Abstract.** A novel processing technique was developed to produce an *in-situ* nano-composite powder based on  $\text{La}_{0.6}\text{Sr}_{0.4}\text{Co}_{0.2}\text{Fe}_{0.8}\text{O}_{3-\delta}$  (LSCF6428) and  $\text{Gd}_{0.1}\text{Ce}_{0.9}\text{O}_{1.95}$  (GDC10) for application as cathode material in intermediate temperature solid oxide fuel cells (IT-SOFC). The nano-composite powder was produced using glycine-nitrate solution combustion technique starting from nitrates of six metal ions. The synthesized powder was characterized using X-ray diffraction (XRD), transmission electron microscopy (TEM), particle size and BET surface area analyses. XRD analysis of as-produced nano-composite powder confirmed the formation of desired phases right after combustion synthesis. The structural parameters of different phases present in the powders were estimated through Rietveld refinement of XRD data. To compare the electrical properties of nano-composite cathode powder produced through the present method, nano-powders of GDC10 and LSCF6428 were individually produced through glycine nitrate process and subsequently mixed through solid-state technique and characterized for functional properties. Using this *in-situ* nano-composite material, lower polarization resistance was achieved as compared to the LSCF–GDC composite produced from mechanical mixtures of nano-powders of GDC10 and LSCF6428 when used as cathode in GDC10 electrolyte-based symmetrical cell. The effects of cathode layer thickness and electrode firing temperature on the cathodic polarization resistance were studied using *in-situ* nano-composite cathode powder.

**Keywords.** IT-SOFC; electrode; LSCF; perovskite; nano-composite; ac-impedance spectroscopy.

## 1. Introduction

Solid oxide fuel cells (SOFCs) are one of the clean, no-emission technologies known to generate electricity through an electrochemical process. As the efficiency of a fuel cell is not limited by the Carnot cycle, its energy output easily surpasses the conventional energy generation technologies [1]. However, the degradation of cell components of SOFC at higher operating temperatures (800–1000°C) limits its performance [2]. This also hinders its ability to replace the conventional power generation technologies for commercial usage [3]. The degradation problems of SOFCs can be circumvented by reducing the operating temperature of SOFC that leads to development of intermediate temperature SOFCs (IT-SOFC) that operate in 600–800°C temperature range [4]. However, when operating SOFC at such temperatures, one of the most important challenges that needs to overcome is to minimize the cell resistance. The ohmic resistance offered by electrolyte is negligible as compared to polarization resistances offered by the electrodes. It has been observed that majority of the cell resistance is attributed to the polarization resistance that stems from

cathode–electrolyte interface and hence, the reduction of cathodic polarization resistance is crucial to achieve an overall high efficiency and energy output in a fuel cell system [5].

One of the common and well-studied cathode materials for IT-SOFC is based on doubly (Sr, Co) doped perovskite-based lanthanum ferrate with composition  $\text{La}_{0.6}\text{Sr}_{0.4}\text{Co}_{0.2}\text{Fe}_{0.8}\text{O}_{3-\delta}$ , also known as LSCF6428. Cathode material based on LSCF6428 composition exhibits considerable mixed electronic–ionic conductivities (MIEC), high thermal stability and compatibility with ceria-based electrolyte [6]. It has been observed that GDC–LSCF nano-composite offers significantly lower polarization resistance as compared to LSCF cathode [7]. Addition of GDC by 50 vol% to LSCF resulted in 10 times drop in the polarization resistance due to extension of triple phase boundary (TPB) from electrode–electrolyte interface to the entire electrode [8]. Further, cathode material based on LSCF–GDC nano-composite plays an important role in providing desirable thermal expansion coefficient and mechanical stability with GDC-based electrolyte [9]. Therefore, LSCF–GDC nano-composite is a promising cathode material for IT-SOFC.

In the present investigation, a simplified processing technique has been developed to produce an *in-situ* LSCF–GDC nano-composite powder based on  $\text{La}_{0.6}\text{Sr}_{0.4}\text{Co}_{0.2}\text{Fe}_{0.8}\text{O}_{3-\delta}$  (LSCF6428) and  $\text{Gd}_{0.1}\text{Ce}_{0.9}\text{O}_{1.95}$  (GDC10) for application as cathode material in IT-SOFC. The nano-composite LSCF–GDC powder was produced using glycine-nitrate combustion technique starting from nitrates of constituent metal ions. The physical and electrochemical properties of as prepared *in-situ* LSCF–GDC composite were compared with LSCF–GDC composite prepared through solid state mixing of nano-powders of GDC10 and LSCF6428 that were individually synthesized through glycine-nitrate process. The effect of cathode layer thickness and sintering temperature on the cathode polarization resistance were studied using *in-situ* nano-composite cathode powder.

## 2. Materials and methods

### 2.1 Materials

$\text{La}_{0.6}\text{Sr}_{0.4}\text{Co}_{0.2}\text{Fe}_{0.8}\text{O}_{3-\delta}$  (LSCF6428) and  $\text{Gd}_{0.1}\text{Ce}_{0.9}\text{O}_{1.95}$  (GDC10) powders were individually prepared through glycine-nitrate combustion synthesis technique. The flow-sheet of preparation of these two oxides is shown in figure 1. For preparation of LSCF powder, lanthanum nitrate ( $\text{La}(\text{NO}_3)_3 \cdot 6\text{H}_2\text{O}$ , 99.9% purity, IRE Ltd., India), strontium nitrate ( $\text{Sr}(\text{NO}_3)_2$ , 99.9% purity, Merck Specialities Private Limited, India), ferric nitrate ( $\text{Fe}(\text{NO}_3)_3 \cdot 9\text{H}_2\text{O}$ , GR grade, Loba Chemie Private Limited, India) and cobalt acetate tetrahydrate ( $(\text{CH}_3\text{COO})_2\text{Co} \cdot 4\text{H}_2\text{O}$ , 99% purity, Merck Specialities Private Limited, India) were utilized as starting materials. The solution containing metal ions was complexed with stoichiometric quantity of glycine (AR grade, Merck Specialities Private Limited, India), which acted as fuel during the combustion synthesis. The dehydration of mixed solution, on a laboratory hot plate, resulted in the formation of viscous transparent gel and subsequently converted into black coloured powder through flame combustion. For preparation of GDC10 powder, gadolinium nitrate solution (IRE Ltd., India, 99.9% purity) and cerium nitrate (LR grade, 99.9% purity, Prabhat Chemicals, India) and glycine as fuel were utilized. The as-produced LSCF and GDC powders were taken in the ratio 1:1 by weight and wet mixed on a roller mill for 24 h using zirconia balls using ethanol as mixing medium. The resulting composite powder was dried in an oven for 2 h. The mixed composite electrode powder will be denoted hereafter as LSCF–GDC-MIX.

The *in-situ* LSCF–GDC nano-composite powder was synthesized utilizing the same concept of combustion synthesis route. The flow-sheet of synthesis method is schematically shown in figure 2. All six analytical reagents were used together in the combustion synthesis utilizing glycine as fuel. The metal compounds were taken in the stoichiometric molar ratio that would lead to a composite powder having a nominal phase composition of  $\text{La}_{0.6}\text{Sr}_{0.4}\text{Co}_{0.2}\text{Fe}_{0.8}\text{O}_{3-\delta}$

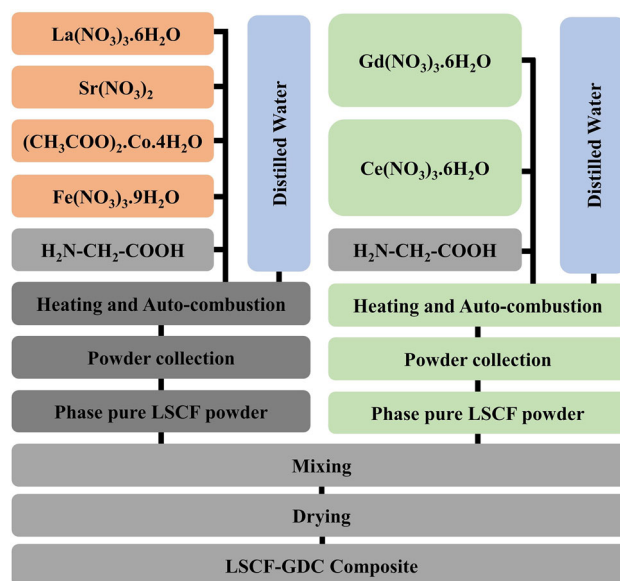


**Figure 1.** Flow-sheet for preparation of  $\text{La}_{0.6}\text{Sr}_{0.4}\text{Co}_{0.2}\text{Fe}_{0.8}\text{O}_{3-\delta}$  (LSCF6428) and  $\text{Gd}_{0.1}\text{Ce}_{0.9}\text{O}_{1.95}$  (GDC10) powders through glycine-nitrate combustion synthesis technique.

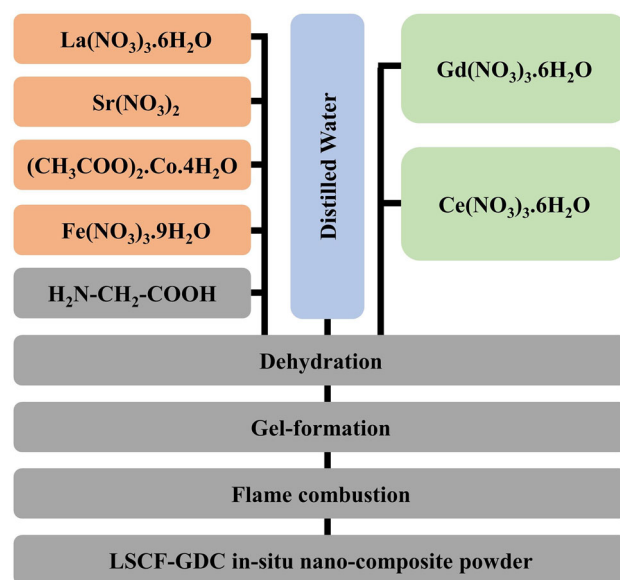


**Figure 2.** Flow-sheet for preparation of *in-situ* nano-composite powder (LSCF–GDC-CS).

(LSCF6428)– $\text{Gd}_{0.1}\text{Ce}_{0.9}\text{O}_{1.95}$  (GDC10) (1:1 ratio by weight). The as-produced nano-composite LSCF–GDC powder hereafter is expressed as LSCF–GDC-CS.

### 2.2 Characterization of powders

The analyses of phase(s) of as-produced GDC10, LSCF6428 and LSCF–GDC-CS powders were carried out using X-ray diffraction (XRD) technique (Panalytical, Xpert-3). The XRD

patterns were recorded at a scan rate of  $0.013^\circ \text{ s}^{-1}$  using  $\text{CuK}\alpha$  radiation. The lattice parameters of the phases present in the powders were determined using Rietveld refinement on XRD data [10]. Rietveld analysis was performed using Fullprof program incorporated in the WinPLOTR software package [11]. In the refinement process, sixth order polynomial function was used to model the background, while pseudo-Voigt function was used to model the profile shape [12]. The crystal structure of phase(s) present in the powders could be visualized through Vesta Software [13], utilizing the structural information obtained through Rietveld refinement. The average crystallite sizes of the crystalline phases present in the as-produced powders were determined from the X-ray line broadening using Scherrer's formula [14].

Transmission electron microscopy (TEM) was performed on as-produced LSCF powder for the evaluation of crystallite size. Identification of crystal structure of the phase present in the powder was studied through the analysis of selected area electron diffraction (SAED) pattern. The sample for TEM analysis was prepared by ultrasonic dispersion of a small quantity of powder in isopropyl alcohol followed by application of dispersed solution on a carbon-coated copper grid. The grid, after drying under IR lamp, was loaded in 300 keV TEM (FEI TEM, Tecnai G2).

The particle size distributions of as-produced GDC, LSCF and LSCF–GDC–CS powders were determined using a dynamic light scattering (DLS) particle size analyser (Zetasizer Nano ZS). Specific surface areas of as-produced powders were examined through BET (Brunauer–Emmett–Teller) technique (Sorptomatic 1990). Based on the assumption that the powder particles are of spherical shape, their average particle diameter could be calculated using BET specific surface area data using the following equation (1):

$$d = \frac{6000}{\rho * S} \quad (1)$$

where  $d$  is the average particle diameter (in nm),  $\rho$  the theoretical density (in  $\text{g cm}^{-3}$ ) and  $S$  the specific surface area ( $\text{m}^2 \text{ g}^{-1}$ ) of the sample.

### 2.3 Consolidation

Green pellets of electrolyte (GDC10) were prepared by uniaxial hydraulic pressing at 150 MPa using a 15 mm diameter die. Stearic acid and alcohol were used as lubricant and cleaning agent, respectively. GDC10 green pellets were sintered at  $1350^\circ\text{C}$  for 4 h. The sintered density of the pellets was evaluated using Archimedes principle. For symmetric cell measurements, sintered GDC10 pellets were utilized, which were subsequently coated with cathode inks. For preparation of cathode inks, both cathode powders (LSCF–GDC–MIX and LSCF–GDC–CS) were mixed separately with terpeneol (1:1 by weight) and the respective inks were brush-coated on both sides of the GDC electrolyte pellets separately, followed by baking at 1000, 1100 and  $1200^\circ\text{C}$  for 1 h.

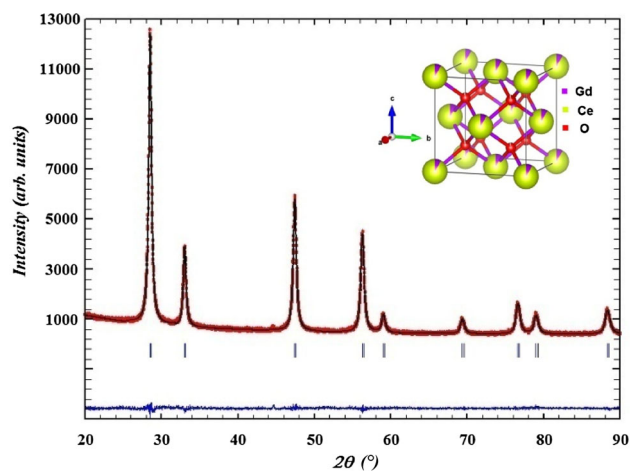


**Figure 3.** Rietveld refinement pattern of as-produced GDC10 powder. The calculated and observed patterns are shown in the top by solid line and dots, respectively. The vertical marks in the middle show positions calculated for Bragg reflections for  $\text{Ce}_{0.9}\text{Gd}_{0.1}\text{O}_{1.95}$  phase. The trace in the bottom is a plot of the difference: observed – calculated.

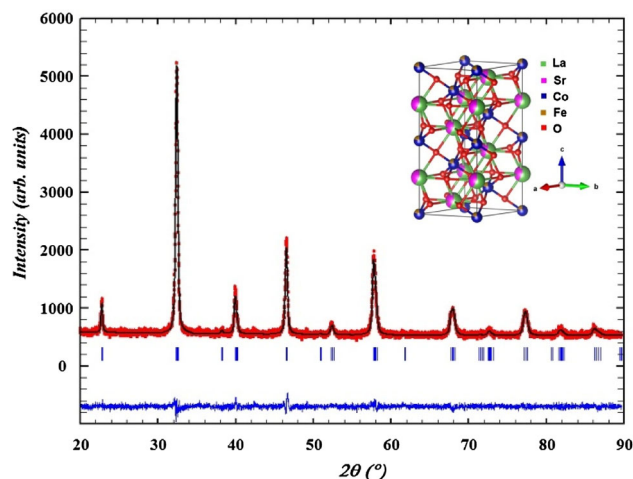
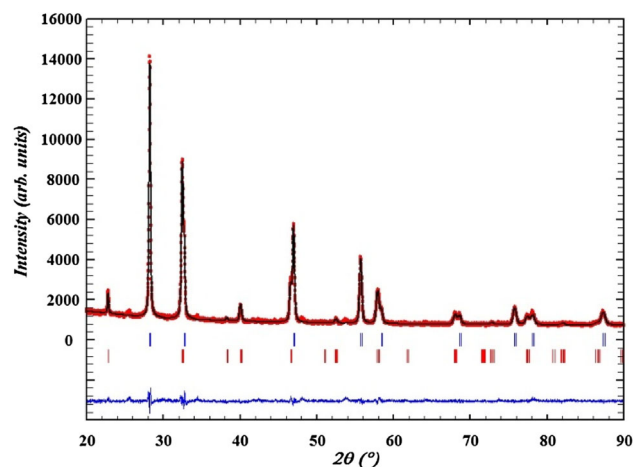
The microstructural analyses of sintered GDC specimen and cross-sectional study of symmetric cells were carried out using scanning electron microscopy (SEM, Zeiss EVO-18). Electrochemical impedance spectroscopy measurements (EIS) were conducted for LSCF–GDC–MIX and LSCF–GDC–CS composites cathode-based symmetric cells using frequency response analyser (Solartron 1260A). A platinum mesh was used as current collector during the measurements. The impedance measurement was performed under cooling cycle  $800\text{--}400^\circ\text{C}$  in steps of  $50^\circ\text{C}$  with frequency swept from 100 kHz to 0.1 Hz with 10 mV amplitude excitation signal. The output results were recorded with ZPlot impedance measurement software and the cathode polarization resistances at different temperatures were evaluated with the help of commercial ZView impedance analysis software [15].

### 3. Results

Figure 3 shows the Rietveld refinement pattern of as-synthesized GDC10 powder. The tick marks below the patterns represent the positions of all possible Bragg reflections. The lower solid line represents the difference between the observed and calculated intensities. The refined lattice parameter and cell volume of GDC10 along with the reliability factors of Rietveld refinement are provided in table 1. The quality of the agreement between observed and calculated profiles is evaluated by profile factor ( $R_p$ ), weighed profile factor ( $R_{wp}$ ), expected weighed profile factor ( $R_{exp}$ ) and reduced chi-square ( $\chi^2$ ). The mathematical expressions of the above parameters can be found elsewhere [10]. The reliability parameters obtained through this refinement are  $R_p$ : 2.80%;  $R_{wp}$ : 3.76%;  $R_{exp}$ : 3.36%;  $\chi^2$ : 1.25. The values of the reliability parameters guarantee the reliability of

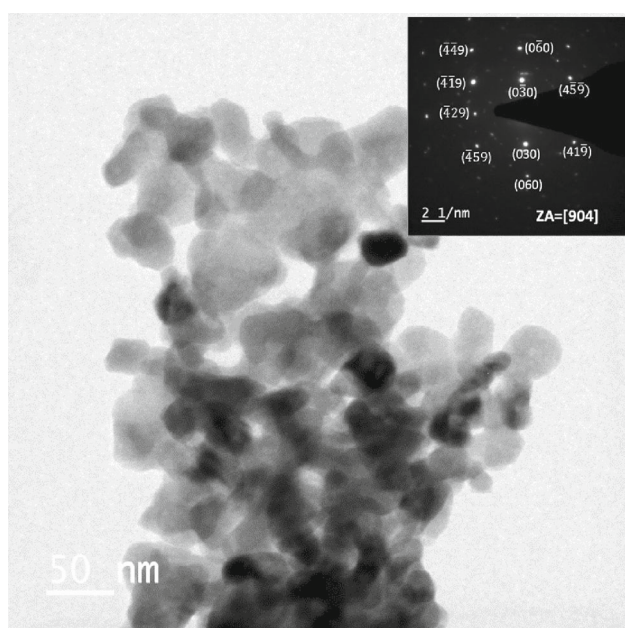
**Table 1.** Structural parameters of GDC10, LSCF and GDC–LSCF–CS powders.

Powder	Phase	Space group	Lattice parameter (Å)	CD (Å <sup>3</sup> )	Reliability factors of Rietveld refinement			
					$R_p$	$R_{wp}$	$R_{exp}$	$\chi^2$
GDC10	Gd <sub>0.1</sub> Ce <sub>0.9</sub> O <sub>1.95</sub>	Fm-3m	5.41773 (12)	159,02 (1)	2.80	3.76	3.36	1.25
LSCF6428	La <sub>0.6</sub> Sr <sub>0.4</sub> Co <sub>0.2</sub> Fe <sub>0.8</sub> O <sub>3-δ</sub>	R-3c	$a = b = 5.5297$ (3) $c = 13.4634$ (11) $\alpha = \beta = \gamma = 90^\circ$	356,53 (4)	3.70	4.65	3.98	1.37
LSCF-GDC-CS	Gd <sub>0.1</sub> Ce <sub>0.9</sub> O <sub>1.95</sub>	Fm-3m	$a = 5.46998$ (14)	163,665 (7)	3.22	4.12	2.99	1.90
	La <sub>0.6</sub> Sr <sub>0.4</sub> Co <sub>0.2</sub> Fe <sub>0.8</sub> O <sub>3-δ</sub>	R-3c	$a = b = 5.5181$ (4) $c = 13.4737$ (18) $\alpha = \beta = \gamma = 90^\circ$	355,30 (6)				

**Figure 4.** Rietveld refinement pattern of as-produced LSCF powder. The calculated and observed patterns are shown in the top by solid line and dots, respectively. The vertical marks in the middle show positions calculated for Bragg reflections for La<sub>0.6</sub>Sr<sub>0.4</sub>Co<sub>0.2</sub>Fe<sub>0.8</sub>O<sub>3-δ</sub> phase. The trace in the bottom is a plot of the difference: observed – calculated.**Figure 5.** Rietveld refinement pattern of as-produced GDC–LSCF–CS powder. The calculated and observed patterns are shown in the top by solid line and dots, respectively. The vertical marks in the middle show positions calculated for Bragg reflections GDC10 and LSCF6428 phases. The trace in the bottom is a plot of the difference: observed – calculated.

refinements. The lattice parameter of GDC10 obtained after Rietveld refinement (5.41773 Å) is in good agreement with the reported value of fluorite phase (5.418 Å) for Ce<sub>0.9</sub>Gd<sub>0.1</sub>O<sub>1.95</sub> composition (ICDD PDF: 01-075-0161) [16]. The inset of figure 3 shows the fluorite structure of GDC derived from structural parameters obtained through Rietveld refinement. The XRD result suggests that desired phase of GDC could be obtained immediately after the combustion reaction and it does not call for any subsequent calcination step for phase formation.

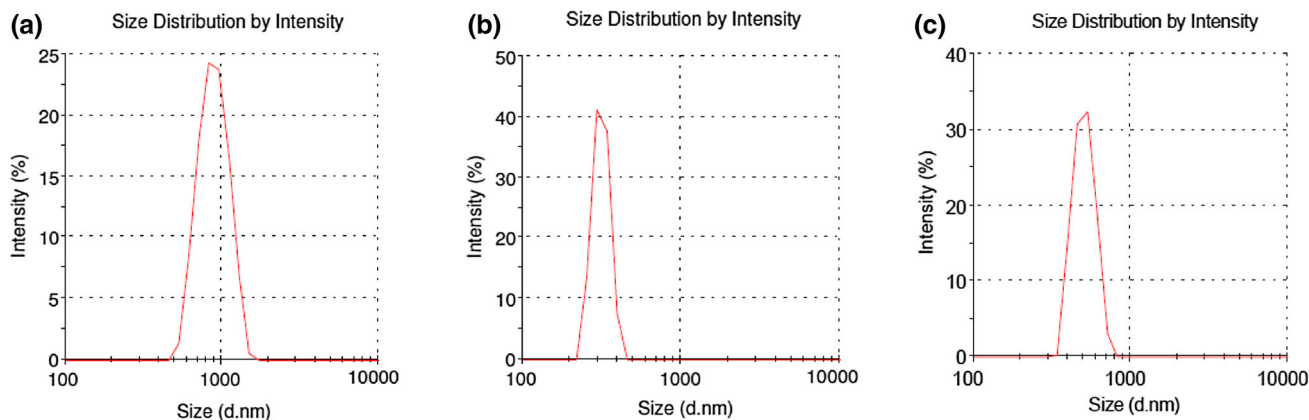
Figure 4 shows Rietveld refinement pattern of the as-synthesized LSCF powder produced through combustion reaction. The refined lattice parameters and cell volume of LSCF along with the reliability factors of Rietveld refinement are given in table 1. LSCF powder crystallizes in rhombohedral structure (space group: R-3c). The refined lattice parameters of LSCF match closely with that of reported values for LSCF of same composition (ICDD PDF: 00-048-0124). The inset of figure 4 shows the rhombohedral crystal structure of LSCF derived from structural parameters obtained through Rietveld refinement. The XRD result of LSCF powder indicates that nano-crystalline powder with rhombohedral polymorph of LSCF could be obtained after the flame combustion reaction.



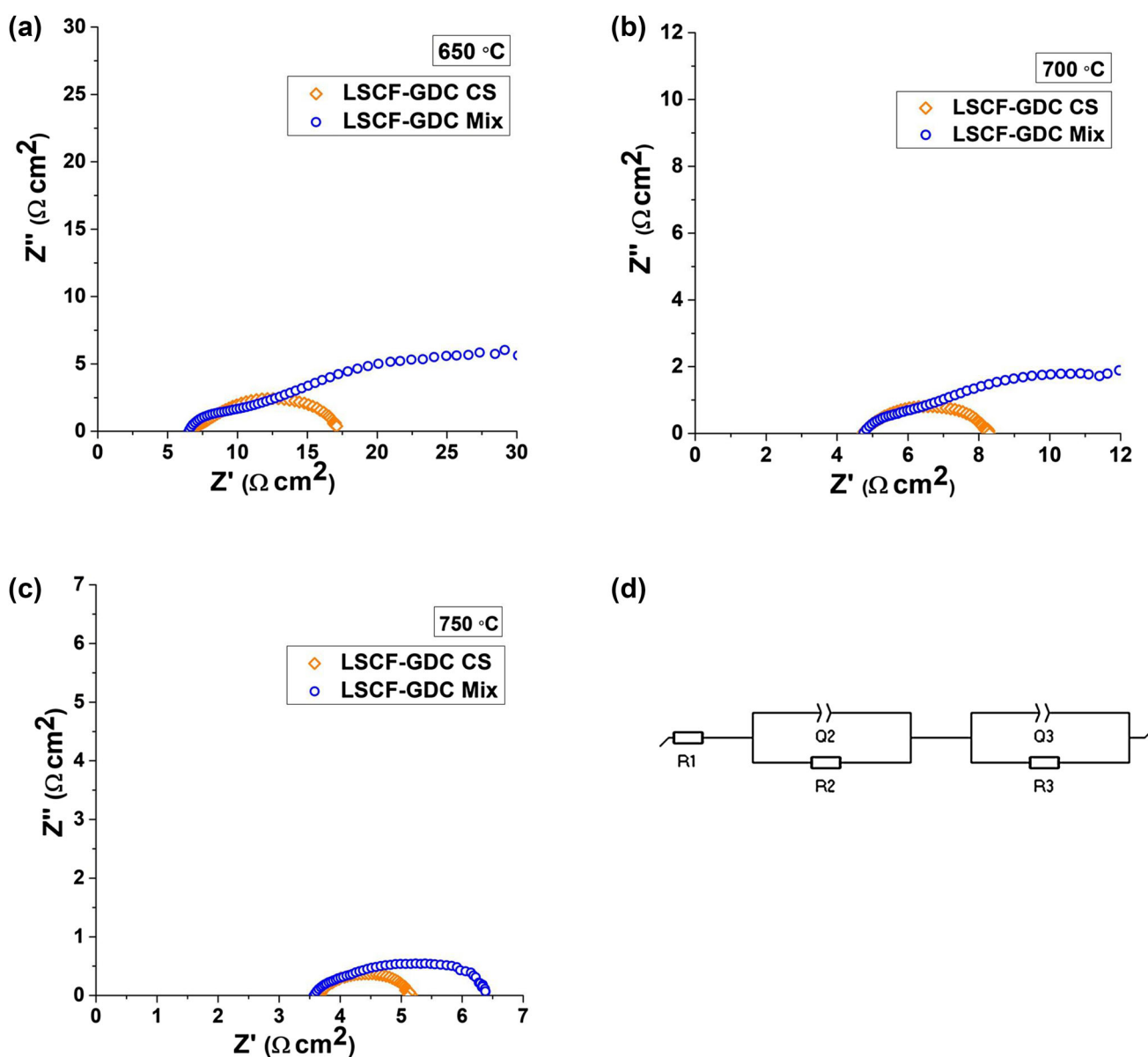
**Figure 6.** TEM photomicrograph of LSCF powder. The inset of the figure shows SAED pattern of LSCF rhombohedral phase.

Figure 5 exhibits the Rietveld refinement pattern of as-synthesized LSCF–GDC–CS powder. In this XRD pattern, reflections corresponding to GDC and LSCF phases were observed. It can be observed from the pattern that two phases (GDC and LSCF) crystallized as a result of combustion synthesis starting from a solution of six metal components. A quantitative two phase Rietveld analysis was performed on XRD pattern of LSCF–GDC–CS powder, which resulted in the determination of lattice parameters of GDC and LSCF phases along with the respective fractions in the pattern. The results of the quantitative Rietveld analysis are given in table 1.

It can be observed from the table that the lattice parameter of GDC phase in LSCF–GDC–CS powder is 0.96% larger than that of GDC10 phase produced in the present investigation using glycine nitrate route. The accompanying cell volume increase in GDC phase of LSCF–GDC–CS powder is 2.92% as compared to that of GDC10 phase. The results show that solubility of metal cation(s) in GDC from the LSCF phase. Since the ionic radii of B site cations (Co, Fe) of LSCF are substantially smaller than the ionic radius of  $\text{Ce}^{+4}$ , it is unlikely that they have substituted the cerium site that have resulted in increase in the value of lattice parameter of GDC unit cell. The ionic radius of  $\text{La}^{+3}$  is 1.16 Å, whereas the ionic radius of  $\text{Ce}^{+4}$  is 0.97 Å for coordination number 8 [17]. This means that the ionic radius of  $\text{La}^{+3}$  is 19.59% bigger than  $\text{Ce}^{+4}$  and hence, its partial substitution at cerium site would increase the lattice parameter of GDC unit cell. Similar substitution of  $\text{La}^{+3}$  at the place of  $\text{Ce}^{+4}$  has been observed during sintering of GDC–LSCF composite at higher temperatures [18,19]. The substitution of La at the site of cerium results in formation of lanthanum-deficient LSCF with a lattice parameter slightly lower than the lattice parameter of LSCF phase when produced separately. Similar trend has been observed in the present investigation, where the lattice parameters ( $a$  and  $b$ ) of LSCF phase in nano-composite is slightly lower than the phase of same composition when it was prepared separately. The results of the quantitative analysis show that the fraction



**Figure 7.** Particle size distributions of (a) GDC10; (b) LSCF and (c) LSCF–GDC–CS powders.



**Figure 8.** Nyquist plots for symmetrical cell utilizing LSCF–GDC–CS and LSCF–GDC–MIX at (a) 650, (b) 700, (c) 750 and (d) equivalent circuit for fitting the EIS data.

of GDC and LSCF phases in the powders are  $47.57 \pm 0.84$  and  $52.43 \pm 1.81\%$ , respectively, which is very close to that of the nominal composition (1:1 by wt) of the powder.

The crystallite sizes of GDC10, LSCF as calculated from XRD data are 14.82 and 22.5 nm, respectively, while in GDC–LSCF–CS nano-composite, the crystallite size of GDC and LSCF phases, calculated from the non-overlapping strongest peaks of the respective phases, are 27 and 24 nm, respectively. The TEM photomicrograph of as produced LSCF powder is shown in figure 6. The powder is composed of nano-particles with an average crystallite size of less than 30 nm, which corroborates the XRD data about nano-crystallinity of powder particles. The SAED pattern of the powder is shown in the inset of figure 6, which shows the spot patterns corresponding

to rhombohedral crystal structure of LSCF phase. The particle size distributions of GDC10, LSCF and LSCF–GDC–CS powders are shown in figure 7. The average particle size of LSCF powder was found to be 315 nm, whereas average particle size of GDC10 was 896 nm. The results suggest that these powder particles are agglomerated, the degree of agglomeration is greater in GDC than in LSCF powder. The average particle size of LSCF–GDC–CS powder was 510 nm, which is intermediate between the average particle size distributions of GDC and LSCF produced through combustion synthesis route.

Figures 8a–c show the Nyquist plots for LSCF–GDC–MIX- and LSCF–GDC–CS-based symmetric cells at 650, 700, 750 °C. The impedance data were fitted using equivalent

**Table 2.** Polarization resistance ( $\Omega \text{ cm}^2$ ) of LSCF–GDC–CS cathode at different operating temperatures as a function of cathode firing temperature.

Cathode firing temperature ( $^{\circ}\text{C}$ )	Measuring temperature ( $^{\circ}\text{C}$ )			
	650	700	750	800
1000	9.58	3.18	1.06	0.38
1100	5.48	1.82	0.79	0.35
1200	4.22	1.33	0.48	0.17

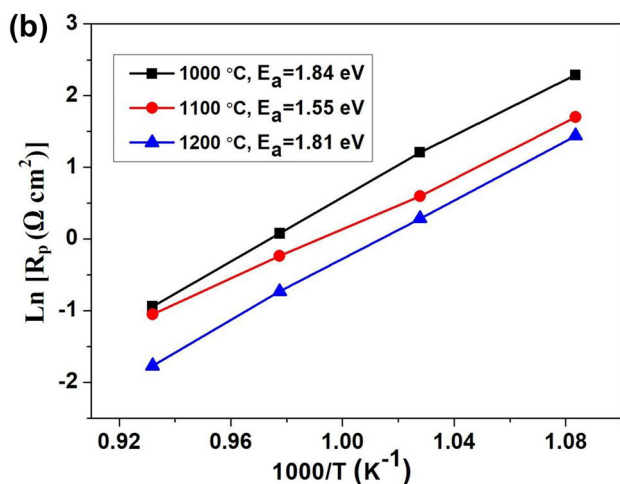
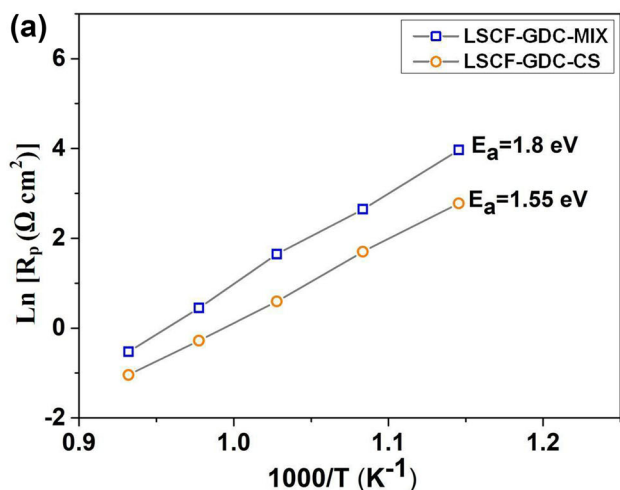


**Figure 9.** Arrhenius plots as a function of polarization resistance and the inverse of temperature for (a) LSCF–GDC–CS and LSCF–GDC–MIX and (b) LSCF–GDC–CS at different sintering temperatures.

circuit (shown in figure 8d) by using a standard commercial software. The equivalent circuits were consisting of a series ohmic resistance ( $R_1$ , which represents resistivity arising from electrolyte, current collectors, lead wires, etc.) and two

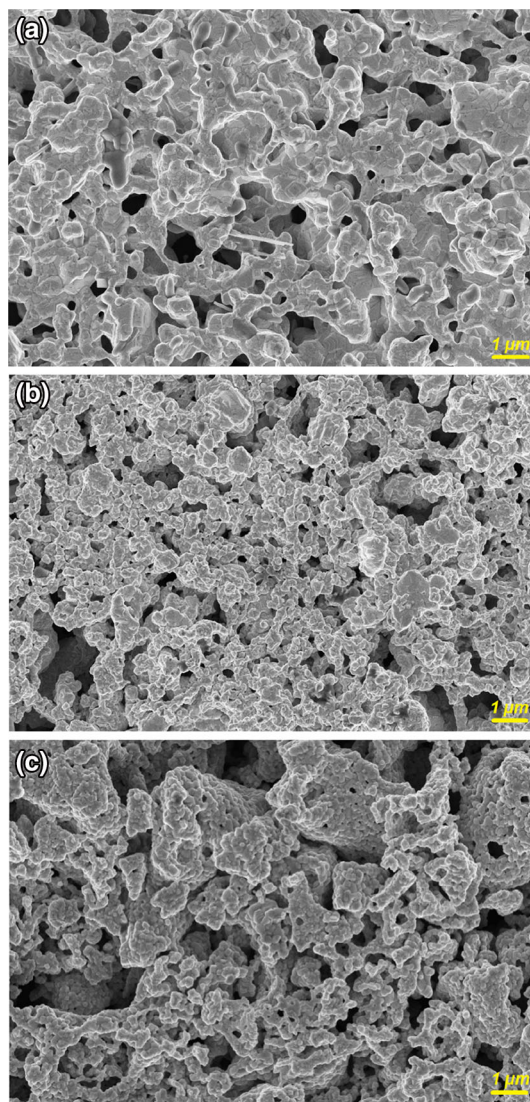


**Figure 10.** SEM photomicrographs of (a) LSCF, (b) LSCF–GDC–MIX and (c) LSCF–GDC–CS cathode materials.

standard resistor-constant phase element (R-CPE) units (R2-Q2 and R3-Q3). The total cathodic polarization resistances for the symmetric cell measurements were calculated from the values of  $R_2$  and  $R_3$ . After being normalized with respect to the area of electrode, the polarization resistance ( $R_p$ ) is presented using the unit  $\Omega \text{ cm}^2$ . The obtained values of  $R_p$  from the fitted circuit have been tabulated in table 2. It could be observed that the cathode polarization resistance offered by LSCF–GDC–CS is lower than that of LSCF–GDC–MIX for all the temperatures of investigation. Figure 9 shows Arrhenius plot exhibiting the variations of polarization resistance as a function of inverse temperature for both the cathode materials. The activation energy offered by LSCF–GDC–MIX was found to be higher than that of LSCF–GDC–CS. The figure shows that under the present experimental conditions, LSCF–GDC–CS is a better cathode material than LSCF–GDC–MIX. To study the effect

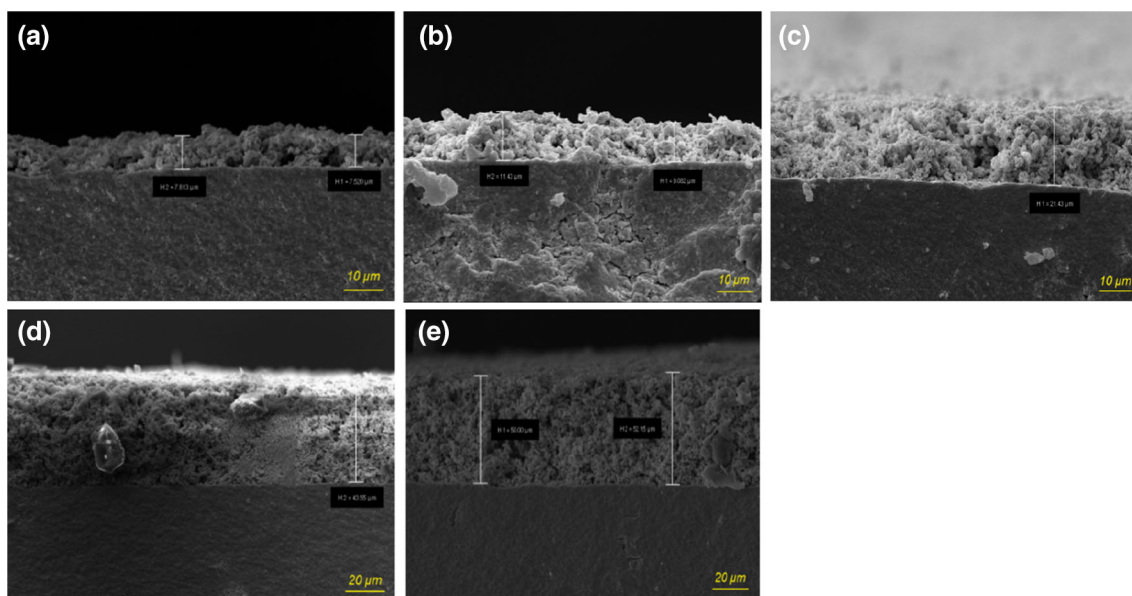


**Figure 11.** (a–e) SEM photomicrographs of symmetric cells with various cathode layer thicknesses.

of firing temperature on polarization resistance offered by LSCF–GDC–CS cathode, the GDC10 based symmetric cells with LSCF–GDC–CS electrode were fired at different temperatures in the range between 1000 and 1200°C. Table 2 shows the variations of polarization resistance offered by LSCF–GDC–CS cathode at different operating temperatures as a function of cathode firing temperature. It was observed that the polarization resistance of the cathode decreased with increase in firing temperature in the range of 1000–1200°C. LSCF–GDC–CS cathode material exhibited a polarization resistance of 0.48 and 0.17  $\Omega \text{ cm}^2$  at 750 and 800°C, respectively, when fired at 1200°C. The reduction of polarization with increase in firing temperature suggests that the evolution of electrode microstructure is not complete at lower firing temperature, which results from the relatively poor contacts between the cathode particles.

Typical microstructures of LSCF, LSCF–GDC–MIX and LSCF–GDC–CS cathodes on the symmetric cells fired at 1100°C for 1 h are shown in figure 10a, b and c, respectively. The micrographs exhibit uniform macro- and micro-pores, which is one of it's the most desirable properties to allow for sufficient gas intake and thereby reducing the chances of resistance due to concentration polarization.

To study the effect of cathode layer thickness on the cathodic polarization resistance, GDC10-based symmetric cells were fabricated with various cathode layer thicknesses utilizing LSCF–GDC–CS nano-composite cathode material. SEM photomicrographs of symmetric cells with various cathode layer thicknesses are shown in figure 11a–e. The polarization resistance of these symmetric cells were measured by ac impedance spectroscopy in air. Figure 12 shows the variation of polarization resistance of LSCF–GDC–CS as a function of cathode layer thickness at 650°C. The data values for polarization resistance ( $R_p$ ) as a function of electrode

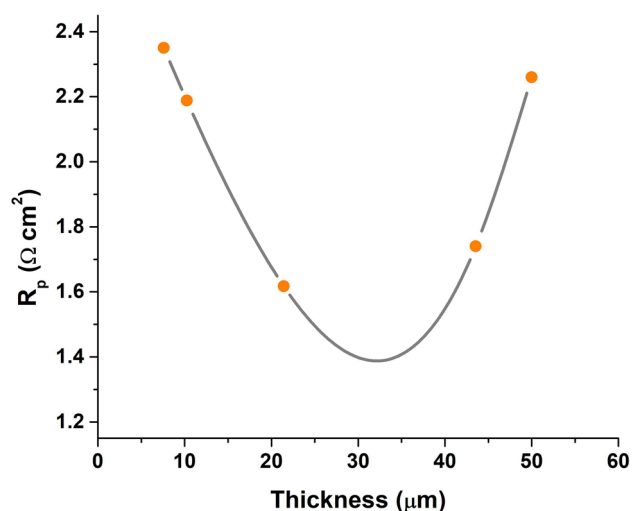


**Figure 12.** Plot showing variations of polarization resistance of LSCF–GDC–CS cathode as a function of cathode layer thickness on GDC10 electrolyte supported symmetric cell measured at 650°C.

thickness were interpolated using spline interpolation function to achieve the best possible fit. Based on this interpolation fitting, it can be estimated that the minimum polarization resistance for LSCF–GDC–CS cathode lies in the range of 22–44  $\mu\text{m}$ . Zhao *et al* [20] observed the similar trend in cathodic polarization resistance as a function of electrode layer thickness for tubular SOFC. Increasing the cathode layer thickness within a certain limit enhances surface oxygen exchange process, oxygen diffusion and adsorption processes; however, further increase in electrode layer thickness induces higher area specific resistance originating from the slow diffusion process.



#### 4. Conclusions

For application as cathode material for IT-SOFC, an *in-situ* nano-composite powder comprising of GDC10 and LSCF6428 phases was synthesized using a combustion-based technique that resulted in the formation of desired phases immediately after the flame-combustion process. The polarization resistance offered by this nano-composite was found to be lower than that of LSCF–GDC composite cathode powder prepared by mechanical mixture of GDC10 and LSCF6428 nano-powders. The variation of polarization resistance offered by the developed composite cathode was studied as a function of cathode layer thickness. The process parameters were optimized that resulted in the minimization of polarization resistance of the nano-composite cathode utilizing GDC-based electrolyte material.

#### Acknowledgements

We thank J Kolte of IIT, Bombay, for his support in XRD measurement of the electrode samples.

#### References

- [1] Song C 2002 *Catal. Today* **77** 17
- [2] Stambouli A B and Traversa E 2002 *Renew. Sustain. Energy Rev.* **6** 433
- [3] Minh N Q 1993 *J. Am. Ceram. Soc.* **76** 563
- [4] Brett D J L, Atkinson A, Brandon N P and Skinner S J 2008 *Chem. Soc. Rev.* **37** 1568
- [5] Xia C and Liu M 2001 *Solid State Ionics* **144** 249
- [6] Yamamoto O 2000 *Electrochim. Acta* **45** 2423
- [7] Maguire E, Gharbage B, Marques F M B and Labrincha J A 2000 *Solid State Ionics* **127** 329
- [8] Murray E P 2001 *Solid State Ionics* **143** 265
- [9] Fleig J 2003 *Annu. Rev. Mater. Res.* **33** 361
- [10] Rietveld H M 1969 *J. Appl. Crystallogr.* **2** 65
- [11] Roisnel T and Rodríguez-Carvajal J 2000 *Materials Science Forum, Proceedings of the seventh European powder diffraction Conference (EPDIC 7)*, p 118
- [12] Thompson P, Cox D and Hastings J 1987 *J. Appl. Crystallogr.* **20** 79
- [13] Vesta (visualization for electronic and structural analysis) 2019 edition. Available: <http://jp-minerals.org/vesta/en/download.html> (accessed on 16 May 2019)
- [14] Patterson A L 1939 *Phys. Rev.* **56** 978
- [15] ZView Software—AMETEK SI; 2017 edition. Available: <http://www.scribner.com/software/68-general-electrochemist-r376-zview-for-windows.html> (accessed on 5 January 2019)
- [16] Brauer G and Gradinger H 1954 *Z. Anorg. Allg. Chem.* **276** 209
- [17] Shannon R D 1976 *Acta Crystallogr. Sect. A* **32** 751
- [18] Izuki M, Brito M E, Yamaji K, Kishimoto H, Cho D H and Shimonosono T 2011 *J. Power Sources* **196** 7232
- [19] Molenda J, Świerczek K and Zajac W 2007 *J. Power Sources* **173** 657
- [20] Zhao K, Kim B H, Norton M G and Ha S Y 2018 *Front. Energy Res.* **6** 1